

## VARIABLE JETS WITH NON-TOP HAT EJECTION CROSS SECTIONS: A MODEL FOR THE KNOTS OF THE HH 34 JET

A. C. Raga,<sup>1</sup> A. Noriega-Crespo,<sup>2</sup> P. Kajdic,<sup>3</sup> F. De Colle,<sup>4</sup> D. López-Cámara,<sup>1</sup> and A. Esquivel<sup>1</sup>

Received 2010 December 15; accepted 2011 May 9

### RESUMEN

Calculamos modelos axisimétricos, con una variación sinusoidal (de un modo) y un perfil de sección recta inicial de velocidad. Encontramos que para cocientes de velocidad borde a centro decrecientes, uno obtiene superficies de trabajo con choques de proa con alas progresivamente más extendidas. Estas alas producen emisión de [S II] que parcialmente llena las regiones entre los nudos en los mapas de emisión predichos. Luego calculamos modelos de 3 modos (con parámetros apropiados para el chorro HH 34), y comparamos los mapas de emisión predichos con imágenes del archivo del HST de HH 34. Encontramos que un modelo con cociente de velocidades borde a centro moderado produce estructuras de nudos con morfologías y variabilidades temporales muy parecidas a las observadas en HH 34.

### ABSTRACT

We compute axisymmetric, single-sinusoidal mode variable ejection models with a non-top hat ejection velocity cross section. We find that for decreasing edge-to-center velocity ratios one obtains internal working surfaces with progressively more extended bow shock wings. These wings produce [S II] emission which partially fills in the inter-knot regions in predicted intensity maps. We then compute 3-mode models (with parameters appropriate for the HH 34 jet), and compare predicted intensity maps with archival HST images of HH 34. We find that a model with a moderate edge-to-center velocity ratio produces knot structures with morphologies and time-variabilities with clear similarities to the observations of HH 34.

*Key Words:* ISM: jets and outflows — ISM: kinematics and dynamics — stars: mass-loss — stars: pre-main sequence

### 1. INTRODUCTION

Rees (1978) first suggested that a variability in the ejection might be responsible for the structure observed in extragalactic jets. This idea was then pursued numerically by Wilson (1984), who modeled extragalactic jets with “twin-lobe” structures.

Raga et al. (1990) proposed an ejection variability as a mechanism for explaining the chains of knots observed along HH jets such as HH 34 (Reipurth et al. 1986) and HH 111 (Reipurth 1989). This proposed model was strengthened by the fact that

later ground-based (Reipurth & Heathcote 1992; Reipurth, Raga, & Heathcote 1992) and HST images (Reipurth et al. 2002, 1997) showed that some of the knots along the HH 34 and HH 111 jets have bow-like morphologies.

This model has been explored analytically (e.g., Cantó, Raga, & D’Alessio 2000) and numerically (e.g., De Colle, Raga, & Esquivel 2008). Different effects in variable ejection jets have been studied, such as:

- different forms of the ejection variability (Hartigan & Raymond 1993; Tesileanu et al. 2009),
- the added presence of a precession (Raga & Biro 1993; Smith & Rosen 2005),
- variable jets with magnetic fields (Gardiner & Frank 2000; De Colle et al. 2008),
- variable jets in a sidewind (Esquivel et al. 2009).

<sup>1</sup>Instituto de Ciencias Nucleares, Universidad Nacional Autónoma de México, Mexico.

<sup>2</sup>Spitzer Science Center, California Institute of Technology, CA, USA.

<sup>3</sup>Instituto de Geofísica, Universidad Nacional Autónoma de México, Mexico.

<sup>4</sup>Astronomy and Astrophysics Department, University of California, Santa Cruz, CA, USA.

In the present paper, we focus on the effect on a variable ejection jet of a non-top hat ejection velocity cross section. An analytic model for the effect of a centrally peaked ejection velocity cross section was presented by Raga, Cantó, & Cabrit (1998). These authors show that for decreasing edge-to-center ejection velocity ratios the internal working surfaces (resulting from the ejection time-variability) become progressively more curved. This effect might produce emitting knots with a closer resemblance to some of the bow-shaped knots observed in HH jets.

Some numerical simulations of variable ejection jets have incorporated a non-top hat ejection velocity cross section. For example, Völker et al. (1999) used a quadratic ejection velocity cross section with a factor of 1/2 edge-to-center velocity ratio in variable ejection models. Some of the more recent papers of this group also describe models which incorporate a (presumably quadratic) non-top hat ejection velocity cross section (Rosen & Smith 2003, 2004; Smith & Rosen 2005) with a edge-to-center velocity ratio of 0.7 or 0.8. Dennis et al. (2008) present constant ejection jet models with a quadratic ejection velocity cross section with an edge-to-center ratio of 0.9. Raga et al. (1998) describe an analytic model for leading and internal working surfaces in jets with arbitrary ejection (density and velocity) cross sections, but only present a single numerical simulation of the leading head of a jet with a quadratic velocity cross section with an edge-to-center velocity ratio of 0.8. Raga et al. (2009) also computed variable jet models with a quadratic velocity cross section, and find that even jets with an edge-to-center velocity ratio of 0.8 differ substantially from initially top hat jets. Finally, the paper of Frank et al. (2000) appears to be the only study of a jet with a non-quadratic radial dependence of the ejection velocity. Somewhat surprisingly, a systematic numerical study of the effect on variable jets of different edge-to-center ejection velocity ratios has not yet been made.

In this paper, we present a set of eight axisymmetric, variable jet models (with a sinusoidal ejection variability) in which we explore the effect of varying the edge-to-center ejection velocity ratio. In order to illustrate the possible relevance of non-top hat cross sections for modelling HH jets, we then present a comparison between intensity maps predicted from the models and red [S II] images of the HH 34 jet.

For this purpose, we compute non-top hat, ejection models with the three-mode sinusoidal variability empirically determined for HH 34 by Raga et al. (2002). We explore a set of different edge-to-center ejection velocity ratios, and compare the pre-

dicted intensity maps with archival HST images of the HH 34 jet.

The paper is organized as follows. In § 2, we give a short description of the archival HST images of HH 34. In § 3, we describe the single-mode, non-top hat jet models. In § 4, we compare the intensity maps predicted from non-top hat, three-mode models with the HST images of HH 34. Finally, the results are summarized in § 5.

## 2. THE ARCHIVAL HST IMAGES OF HH 34

The *Hubble Space Telescope* (HST) Wide Field Planetary Camera 2 (WFPC2) data of HH 34 have been retrieved from the *Hubble Legacy Archive* (HLA), for two epochs (1998 & 2007). The processing of the HLA data uses a new calibration pipeline that includes an improved handling of the UV contamination, bias variations and other artifacts<sup>5</sup>. Furthermore, the WFPC2 HLA data have been resampled onto a uniform grid to correct for geometric distortions, an essential step to determine, for instance, the proper motions of knots along the jet between the two epochs.

The 1998 images were described in detail by Reipurth et al. (2002). The HH 34 archival images from 2007 to our knowledge have not been presented anywhere, and we therefore describe them briefly. The data were obtained during the HST Cycle 16 (October 30, 2007) and belong to program 11179 (PI. P. Hartigan) on the dynamics of clumpy supersonic flows in stellar jets. Like in the 1998 observations (Reipurth et al. 2002) the data were obtained using the standard WFPC2 narrow band filters of H $\alpha$  (F656N) and [S II] $\lambda$  6716+30 (F673N). The final images are the result of multiple co-added exposures (eight for both H $\alpha$  & [S II]) which are used to mitigate the effects of cosmic rays, and with a total integration time of 9600 sec for each filter.

## 3. NON-TOP HAT, SINGLE MODE JETS

We have computed a set of models with a time-dependent ejection velocity of the form:

$$v_j(r, t) = \left[ v_0 + v_1 \sin \left( \frac{2\pi t}{\tau} \right) \right] \left[ 1 - (1 - \sigma) \left( \frac{r}{r_j} \right)^2 \right], \quad (1)$$

where  $t$  is the time,  $r$  is the cylindrical radius (measured across the initial cross section of the jet),  $v_0$  is the mean axial velocity of the jet,  $v_1$  is the half-amplitude of the axial velocity variability and  $\sigma = v_{\text{edge}}/v_{\text{axis}}$  is the ratio between the ejection velocity at the edge of the jet ( $v_{\text{edge}}$ , at  $r = r_j$ ) and

<sup>5</sup>See e.g. [http://hla.stsci.edu/hla\\_faq.html#WFPC2](http://hla.stsci.edu/hla_faq.html#WFPC2).

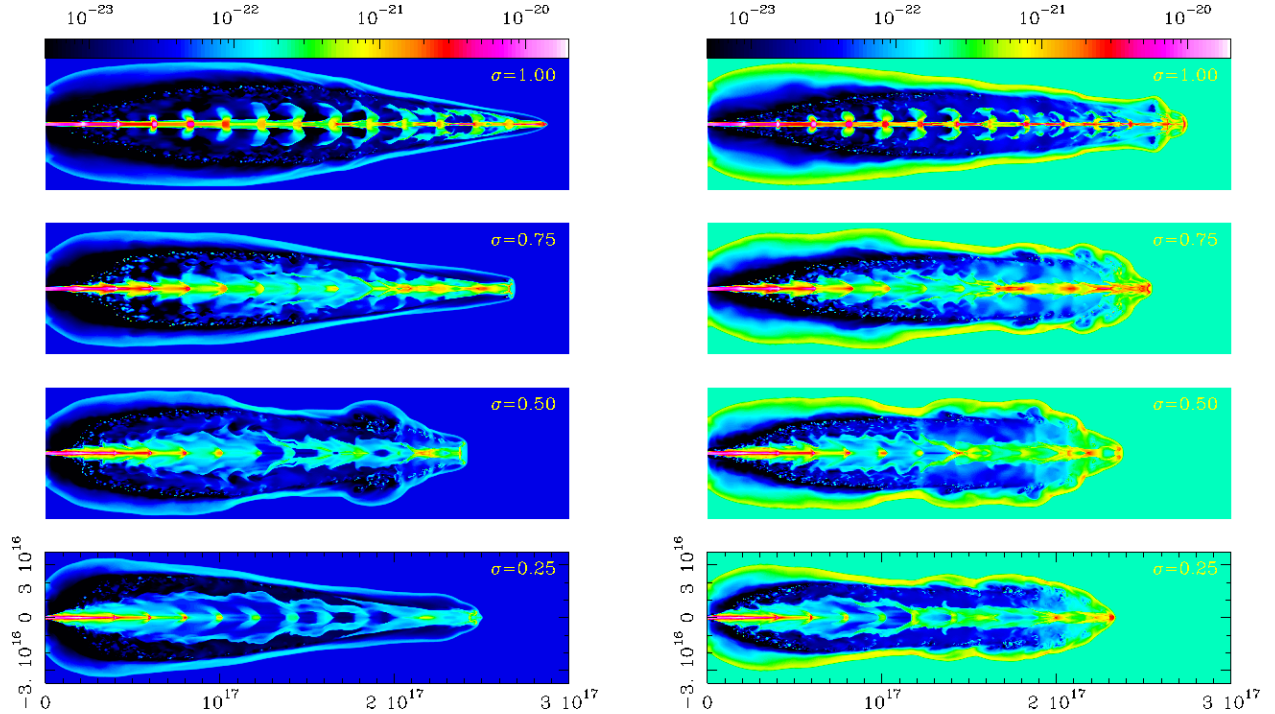


Fig. 1. Density stratifications obtained from the single-sinusoidal mode variable jet models (see § 3). The models of jets moving into an environment with  $n_a = 15 \text{ cm}^{-3}$  are shown at  $t = 350 \text{ yr}$  integration time (left column) and the models with  $n_a = 100 \text{ cm}^{-3}$  are shown at  $t = 400 \text{ yr}$  (right column). The results are labeled with the value of  $\sigma$  (the edge-to-center ejection velocity ratio) of each model. The full computational domain is shown on both sides of the symmetry axis (the axes are labeled in cm). The densities are depicted with the logarithmic color scheme given (in  $\text{g cm}^{-3}$ ) by the top bar. The color figure can be viewed online.

the velocity along the jet axis ( $v_{\text{axis}}$ , at  $r = 0$ ). In other words, the ejection velocity has a single-mode, sinusoidal ejection velocity variability, and a center-to-edge, quadratic radial dependence.

When calculating variable ejection jet models, it is of course possible to include a time-variability in the initial density and/or temperature of the jet. Such variabilities, however, lead to the production of shocks with velocities of the order of the initial sound speed (typically of  $\approx$  a few  $\text{km s}^{-1}$  for HH jets). Because of this, if one wants to model the emission along HH jets (which is formed in shocks with velocities  $\sim 10 \rightarrow 100 \text{ km s}^{-1}$ ), it is clear that an ejection velocity variability with a highly supersonic amplitude has to be included.

We have run two sets of four models (each set corresponding to environments with different densities, see below) with edge-to-center ejection velocity ratios  $\sigma = 1.0$  (top hat), 0.75, 0.5 and 0.25. The models have the same ejection variability, with  $v_0 = 250 \text{ km s}^{-1}$ ,  $v_1 = 30 \text{ km s}^{-1}$  and  $\tau = 30 \text{ yr}$ . The ejection density and temperature have top-hat profiles with  $n_j = 5000 \text{ cm}^{-3}$  and  $T_j = 1000 \text{ K}$  (re-

spectively). For the surrounding, homogeneous environment, we have considered a  $T_a = 1000 \text{ K}$  temperature, and two possible densities:  $n_a = 15$  and  $100 \text{ cm}^{-3}$ . It is assumed that both the jet and the environment are initially neutral except for C and S, which are assumed to be singly ionized. The jets have a  $r_j = 10^{15} \text{ cm}$  initial radius.

The gas-dynamic equations are integrated together with a set of rate equations for H, He, C, N, O and S ions, with an axisymmetric version of the “yguazú-a” adaptive grid code. The resulting, non-equilibrium ionization has been used to compute the energy loss term (included in the energy equation). The version of the code used is identical to the one described in detail by Kajdic, Velázquez, & Raga (2006) and by Raga et al. (2007). For the present calculations, we use a 6-level, binary adaptive grid which would fill the domain with  $4096 \times 512$  (axial  $\times$  radial) points at the highest grid resolution. The cylindrical domain has an on-axis reflection condition, an inflow condition for  $r \leq r_j$  and a reflection condition for  $r > r_j$  on the injection ( $x = 0$ ) plane, and outflow conditions at the remaining two bound-

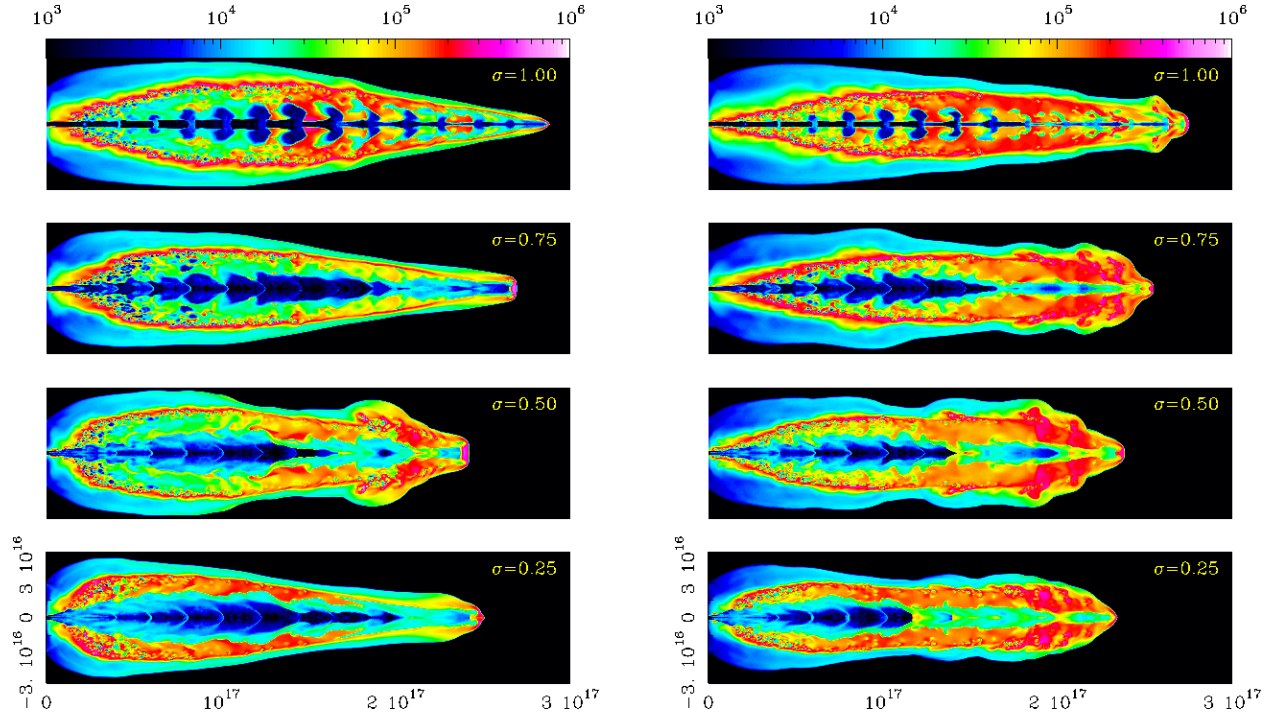


Fig. 2. Temperature stratifications obtained from the single-sinusoidal mode variable jet models (see § 3). The models of jets moving into an environment with  $n_a = 15 \text{ cm}^{-3}$  are shown at a  $t = 350 \text{ yr}$  integration time (left column) and the models with  $n_a = 100 \text{ cm}^{-3}$  are shown at  $t = 400 \text{ yr}$  (right column). The results are labeled with the value of  $\sigma$  (the edge-to-center ejection velocity ratio) of each model. The temperatures are depicted with the logarithmic color scheme given (in K) by the top bar. The color figure can be viewed online.

aries of the  $(30, 3.75) \times 10^{16} \text{ cm}$  (axial  $\times$  radial) computational domain.

The density and temperature stratifications obtained from the four  $n_a = 15 \text{ cm}^{-3}$  models after a  $t = 350 \text{ yr}$  time-integration and the four  $n_a = 100 \text{ cm}^{-3}$  models at  $t = 400 \text{ yr}$  are shown in Figures 1 and 2. The models show a leading jet head and a series of travelling “internal working surfaces” (IWS) which are formed as a result of the ejection time-variability.

We first note that the knots within  $\approx 10^{17} \text{ cm}$  from the source have very similar structures in the  $n_a = 15$  and  $100 \text{ cm}^{-3}$  models. From this, we conclude that the precise value of the environmental density does not have a strong effect on the sequence of knots close to the outflow source (see Figures 1 and 2). It is clear, however, that the value of  $n_a$  does have (as expected) an important effect on the structure and propagation of the leading head of the jet.

On the other hand, it is clear from Figures 1 and 2 that the value chosen for the edge-to-center ejection velocity ratio  $\sigma$  does have a strong effect on the structure of the IWS. For  $\sigma = 1$ , the working

surfaces have compact, dense regions within the jet beam, which eject low density material out into the cocoon of the jet. For lower values of  $\sigma$ , the IWS have clear, bow-shaped morphologies, with densities that fall away from the symmetry axis (see Figure 1).

The value of  $\sigma$  also has a strong effect on the resulting temperature stratifications. For  $\sigma = 1$ , a relatively hot cocoon (with  $T \sim 3 \rightarrow 20 \times 10^4 \text{ K}$ ) is in contact with the jet beam. For lower values of  $\sigma$ , a lower temperature region (with  $T \sim 10^4 \text{ K}$ ) buffers the jet beam from the hot cocoon (this cool region is most clearly seen in the  $\sigma = 0.25$  model, see Figure 2).

In Figure 3, we show the [S II] 6716+6730 emission maps predicted from the four  $n_a = 15 \text{ cm}^{-3}$  models for  $t = 350 \text{ yr}$ . These maps have been computed solving the appropriate 5-level atom problem, and integrating the resulting emission coefficient along lines of sight. It has been assumed that the outflow axis lies on the plane of the sky.

The maps shown in Figure 3 display the region close to the outflow source. It is clear that for  $\sigma = 1$  the emission from the IWS is concentrated in compact “knots”, with only very faint “wings” seen in

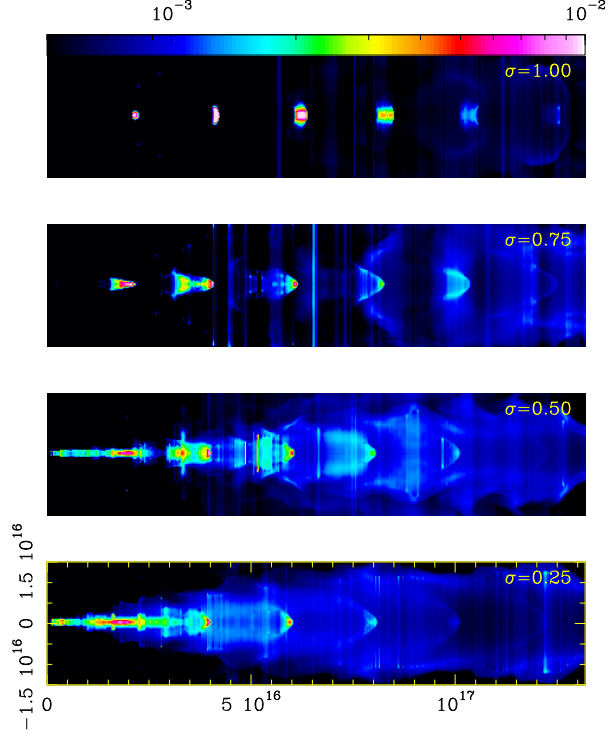


Fig. 3. [S II] 6716+30 intensity maps predicted from the four single-mode jet models with  $n_a = 15 \text{ cm}^{-3}$  (see § 3) for a  $t = 350 \text{ yr}$  integration time. The maps have been computed assuming that the outflow axis lies on the plane of the sky. Only a region close to the jet source is shown (compare with the full computational domain shown in Figures 1 and 2). The intensities are shown with a logarithmic color scheme given (in  $\text{erg s}^{-1} \text{cm}^{-2} \text{sterad}^{-1}$ ) by the top bar. The color figure can be viewed online.

the knots with  $x > 10^{17} \text{ cm}$ . For lower values of  $\sigma$ , the emission knots have bow-wings of increasing intensity. The emission from these bow-wings partially fills in the gaps corresponding to the inter-knot regions (these gaps are clearly seen in the  $\sigma = 1$  model, see Figure 3).

With these models we therefore show that the edge-to-center ejection velocity ratio  $\sigma$  has a strong effect on the morphology of the IWS (which results from the ejection velocity time-variability). For  $\sigma = 1$  (i.e., for a top-hat jet, see equation 1), the [S II] emission of the IWS has a morphology of compact clumps, with low-emission gaps between the clumps. For lower values of  $\sigma$ , the emission from the IWS develops progressively more extended bow wings, which partially fill in the gaps between the successive knots. Therefore, by tuning the value of  $\sigma$  it is possible to produce knots with different mor-

phologies, which could then be compared with the emission observed in specific HH jets. An attempt to do this is presented in the following section.

#### 4. THREE-MODE MODEL FOR HH 34

Raga & Noriega-Crespo (1998) and Raga et al. (2002) proposed a three-mode ejection velocity variability for modelling the structure of the southern lobe of the HH 34 outflow. In particular, Raga et al. (2002) used radial velocity and proper motion observations of HH 34 to derive a variability of the form:

$$v_c(t) = v_0 + v_1 \sin\left(\frac{2\pi t}{\tau_1} + \phi_1\right) + v_2 \sin\left(\frac{2\pi t}{\tau_2} + \phi_2\right) + v_3 \sin\left(\frac{2\pi t}{\tau_3}\right), \quad (2)$$

with  $v_0 = 270 \text{ km s}^{-1}$ ,  $v_1 = 70 \text{ km s}^{-1}$ ,  $\tau_1 = 1400 \text{ yr}$ ,  $\phi_1 = -0.80 \text{ rad}$ ,  $v_2 = 25 \text{ km s}^{-1}$ ,  $\tau_2 = 270 \text{ yr}$ ,  $\phi_2 = -0.85 \text{ rad}$ ,  $v_3 = 10 \text{ km s}^{-1}$  and  $\tau_3 = 27 \text{ yr}$ . This function represents the past time-variability of the ejection of HH 34, with  $t = 0$  representing the present time. Negative values of  $t$  represent the times at which the material presently observed along the HH 34 jet was ejected from the source.

We then choose an ejection velocity  $v_j$  with this three-mode variability, modulated with a quadratic center-to-edge profile:

$$v_j(r, t) = v_c(t) \left[ 1 - (1 - \sigma) \left(\frac{r}{r_j}\right)^2 \right], \quad (3)$$

where  $v_c(t)$  is given by equation (2) and  $\sigma$  is the center-to-edge ejection velocity ratio (see equation 1).

Following Raga et al. (2002), we choose time-independent, top-hat ejection density and temperature cross sections with  $n_j = 5000 \text{ cm}^{-3}$  and  $T_j = 1000 \text{ K}$  (respectively), and a  $r_j = 5 \times 10^{15} \text{ cm}$  jet radius. The jet moves into a homogeneous environment with  $n_a = 15 \text{ cm}^{-3}$  and  $T_a = 1000 \text{ K}$ .

The computational domain has an (axial  $\times$  radial) extent of  $(16.8, 2.1) \times 10^{17} \text{ cm}$ , resolved with  $4096 \times 512$  grid points at the highest resolution of the 6-level, binary adaptive grid. The setup of the three-mode models is otherwise identical to the one of the single-mode models described in § 3.

We have then computed three models, with center-to-edge ejection velocity cross sections with  $\sigma = 1, 0.75$  and  $0.5$ . The simulations were all started at  $t = -3000 \text{ yr}$ , and allowed to evolve until  $t = 300 \text{ yr}$ .

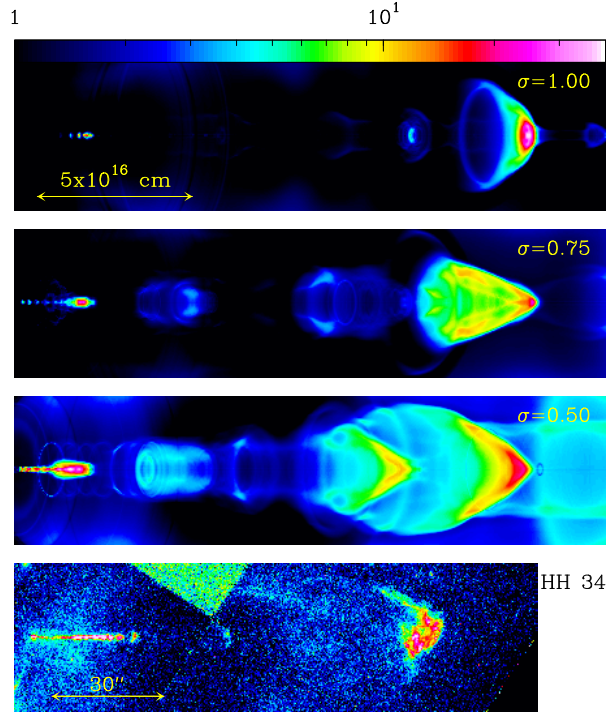


Fig. 4. [S II] 6716+30 intensity maps predicted from the three 3-mode jet models for a time  $t = 0$  (the integration was started at  $t = -3000$  yr, see § 4). The bottom frame shows the [S II] image obtained with the HST in 1998 (see § 2). The predicted maps have been computed assuming that the outflow axis lies at a  $30^\circ$  angle with respect to the plane of the sky (as appropriate for HH 34), and show a  $(10.69, 2.67) \times 10^{17}$  cm domain. The HH 34 [S II] map has been scaled to the same scale as the predicted maps, assuming a distance of 450 pc (the displayed region has a vertical size of  $39''.6$ ). The source of HH 34 is on the left of the chain of aligned knots. The intensities are shown with a logarithmic color scheme covering a dynamic range of 40 (see the top bar), scaled so that in the four maps the brighter regions start to saturate at the highest depicted intensity. The color figure can be viewed online.

In Figure 4, we present the [S II] 6716+30 intensity maps predicted from these three models for  $t = 0$  (i.e., for years  $\sim 1990$ – $1994$  at which the data analyzed by Raga et al. 2002 were obtained). These maps were computed assuming a  $30^\circ$  angle between the jet axis and the plane of the sky, corresponding to the approximate orientation of the HH 34 outflow (see Heathcote & Reipurth 1992). Together with the predicted maps, we show an archival [S II] HST image of the southern lobe of the HH 34 outflow, rotated so that the outflow axis is parallel to the abscissa. The physical size of the domains of the syn-

thetic and observed maps are identical (assuming a 450 pc distance to HH 34).

For all of the computed models, emission structures with a qualitative resemblance to HH 34 are obtained. The four models show a large bow shock at a distance from the source comparable to HH 34S, a chain of knots close to the source, and a few broader, faint condensations between the chain of knots and the large bow shock. These three main features are in qualitative agreement with the observed structure of the HH 34 jet.

It is clear from Figure 4 that the shape of the large bow shock is more flat-topped in the  $\sigma = 1$  model than in the  $\sigma = 0.75$  and  $0.5$  models, in which the bow shock has a more conical morphology. Also, in the  $\sigma = 1$  model (presented previously by Raga et al. 2002), the [S II] emission from the chain of knots is fainter than the emission from the large bow shock. The  $\sigma = 0.75$  and  $0.5$  models show a comparable peak [S II] emission in the main bow shock and in the brighter knots in the chain, in better qualitative agreement with the [S II] image of HH 34.

Figures 5, 6 and 7 show the time-evolution of the [S II] emission of the chain of knots for the  $\sigma = 1$ ,  $0.75$  and  $0.5$  models (respectively), at 100 yr intervals. In the 300 yr time-sequence obtained from the  $\sigma = 1$  model (Figure 5), we see either one or two groups of compact knots. The predicted emission is qualitatively different from the emission from the HH 34 jet (bottom panel), in which the inter-knot regions show considerably brighter emission. Also, some of the observed knots have bow shapes which are not seen in the maps predicted from the  $\sigma = 1$  model.

The time-sequence of [S II] intensity maps obtained from the  $\sigma = 0.75$  model (Figure 6) does show bow-shaped knots. The inter-knot regions show brighter emission, in better qualitative agreement with the HH 34 jet observation.

The emission maps obtained from the  $\sigma = 0.5$  model show groups of knots having less contrast between the knot and inter-knot emission than the HH 34 jet. Because of this, we conclude that the  $\sigma = 0.75$  model produces the best qualitative agreement with the structure of knots along the HH 34 jet. In the following, we therefore focus on the  $\sigma = 0.75$  model.

In Figures 8 and 9 we show a sequence of intensity maps with a time-interval of 10 yr, together with the 1998 and 2007 HST [S II] images (see § 2). From these figures, it is clear that the knots along the HH 34 jets have changed quite strongly over a

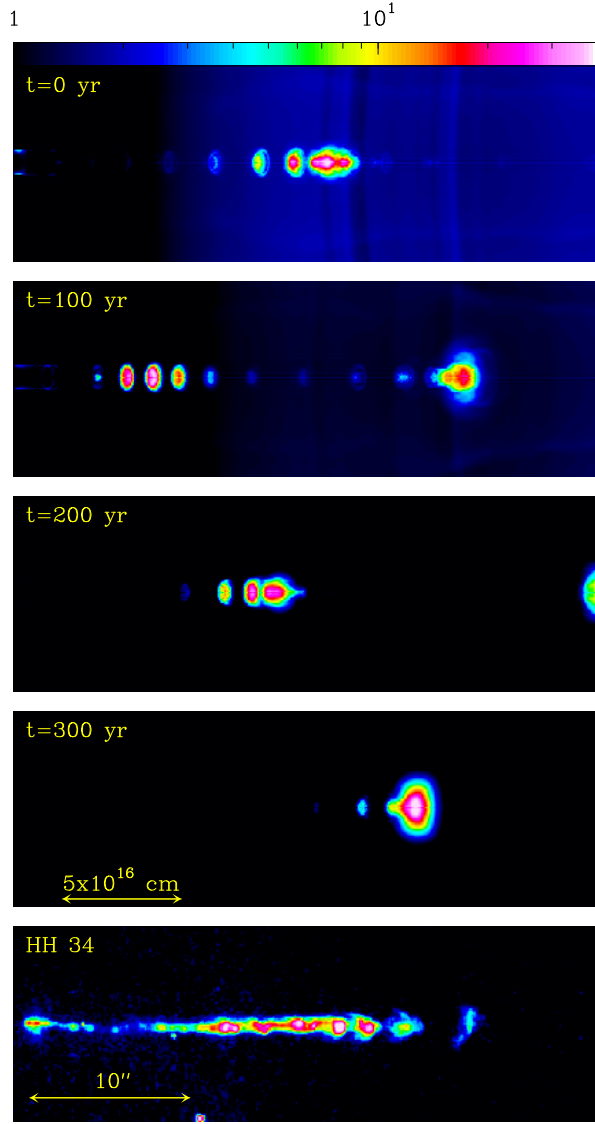


Fig. 5. [S II] 6716+30 intensity maps predicted from the  $\sigma = 1$ , 3-mode jet model for times  $t = 0, 100, 200$  and  $300$  yr (the integration was started at  $t = -3000$  yr, see § 4). The bottom frame shows the [S II] image obtained with the HST in 1998 (see § 2). The predicted maps have been computed assuming that the outflow axis lies at a  $30^\circ$  angle with respect to the plane of the sky (as appropriate for HH 34), and show a region with the source on the left and an axial extent of  $2.46 \times 10^{17}$  cm. The HH 34 [S II] map has been scaled to the same scale as the predicted maps, assuming a distance of 450 pc (the displayed region has a horizontal size of  $36''.5$ ). The intensities are shown with a logarithmic color scheme covering a dynamic range of 40 (see the top bar), scaled so that in the four maps the brighter regions start to saturate at the highest depicted intensity. The color figure can be viewed online.

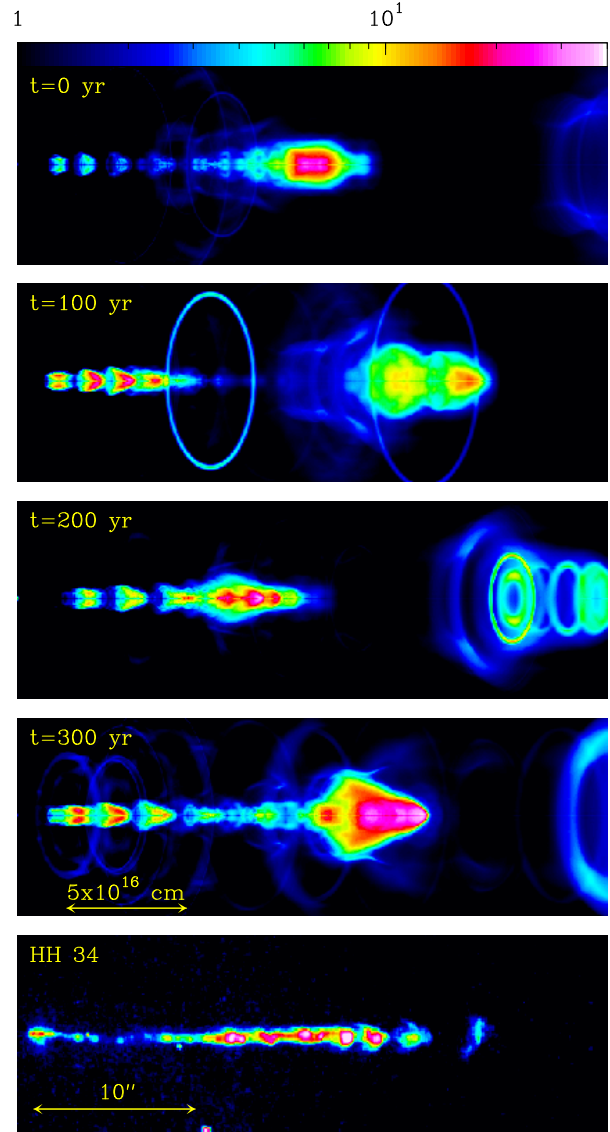


Fig. 6. The same as Figure 5 but for the  $\sigma = 0.75$ , 3-mode jet model (see § 4). The color figure can be viewed online.

13 yr time-span, with some of the knots becoming relatively fainter and other knots becoming brighter.

These changes are clearly seen in Figure 10, which shows intensity vs. position traces (obtained by integrating across the HH 34 jet and subtracting the adjacent background). It is clear that the  $x < 2''$  region (where  $x$  is the distance from the source) has become considerably brighter, that the knots in the  $10'' < x < 30''$  region have had clear variations (several of the knots having become fainter and others brighter).

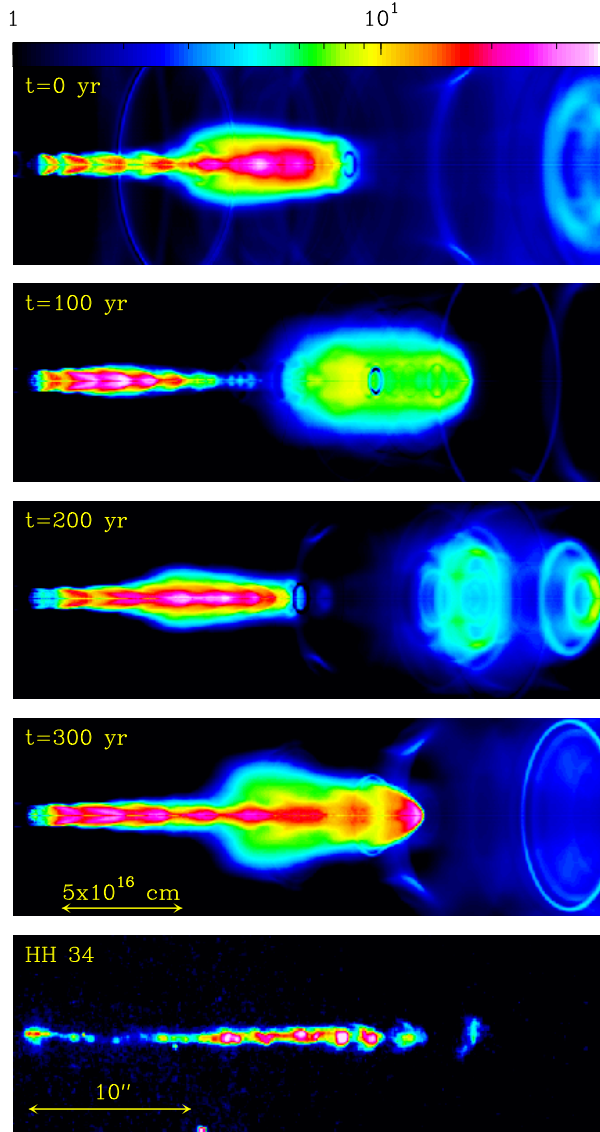


Fig. 7. The same as Figures 5 and 6 but for the  $\sigma = 0.5$ , 3-mode jet model (see § 4). The color figure can be viewed online.

In order to quantify these variations, we have defined segments along the [S II] tracings, incorporating the emission of the better defined knots. The positions and lengths of these segments were defined on the 1998 image (top frame of Figure 10), and were displaced  $0''.7$  in the  $+x$  direction for calculating the knot intensities in the 2007 frame (except for the segment incorporating the emission around the outflow source, which was not displaced). This displacement corresponds to the average motion of the knots along the HH 34 axis between the two epochs (corresponding to a proper motion of  $\approx 170 \text{ km s}^{-1}$ , consistent

with previous measurements of proper motions in this outflow). In the bottom frame of Figure 10, we plot the 2007/1998 intensity ratios for the successive knots (defined above), showing that some of the knots have had intensity variations of up to a factor of  $\sim 2$ .

From Figures 8 and 9 we notice that intensity variabilities similar to the observed ones are also seen in the predicted intensity maps over 10–20 yr time-intervals. For example, from  $t = -60$  to  $t = -50$  yr and  $t = -40$  yr we see that the main knots have intensity changes (with the brightest knot becoming fainter, and some of the other knots brighter). Also, a systematic brightening of the region close to the source is seen from the  $t = 0$  to the  $t = 60$  yr time-frames, with clear changes over each decade.

None of the predicted intensity maps show [S II] emission structures that one could even attempt to compare quantitatively with the HH 34 knots. However, it is clear that several of the time-frames from the model do show structures which resemble the observed knots (see Figures 8 and 9).

## 5. CONCLUSIONS

We have presented a systematic study of the effect of having a non-top hat velocity cross section in the ejection of a variable jet. We have chosen a parabolic velocity cross section, with an edge-to-center velocity ratio  $\sigma = 0.25 \rightarrow 1.0$ .

For a jet with a single-mode, sinusoidal ejection velocity variability (see equation 1), we find that for larger edge-to-center velocity contrasts (i.e., for lower  $\sigma$  values) the internal working surfaces develop bow shapes with progressively more extended wings. These bow wings appear as extensions to the [S II] emission from the knots, filling in the gaps between the knots (see Figure 3).

We then compute a model with the three sinusoidal modes deduced from observations of the HH 34 jet by Raga et al. (2002). We find that a model with  $\sigma = 0.75$  produces a chain of knots close to the source which better resembles the HH 34 [S II] emission than models with  $\sigma = 1$  (i.e., with a top-hat ejection cross section) and with  $\sigma = 0.5$  (this model producing a chain of knots with a too low intensity contrast between the knots and the inter-knot regions).

Finally, we present a time-sequence of the [S II] emission of the knots predicted from the  $\sigma = 0.75$ , three-mode model, and compare the maps with two epochs of HST images of HH 34 (with a  $\approx 10$  yr time interval). We find that the model predicts knot structures with reasonable qualitative similarity to

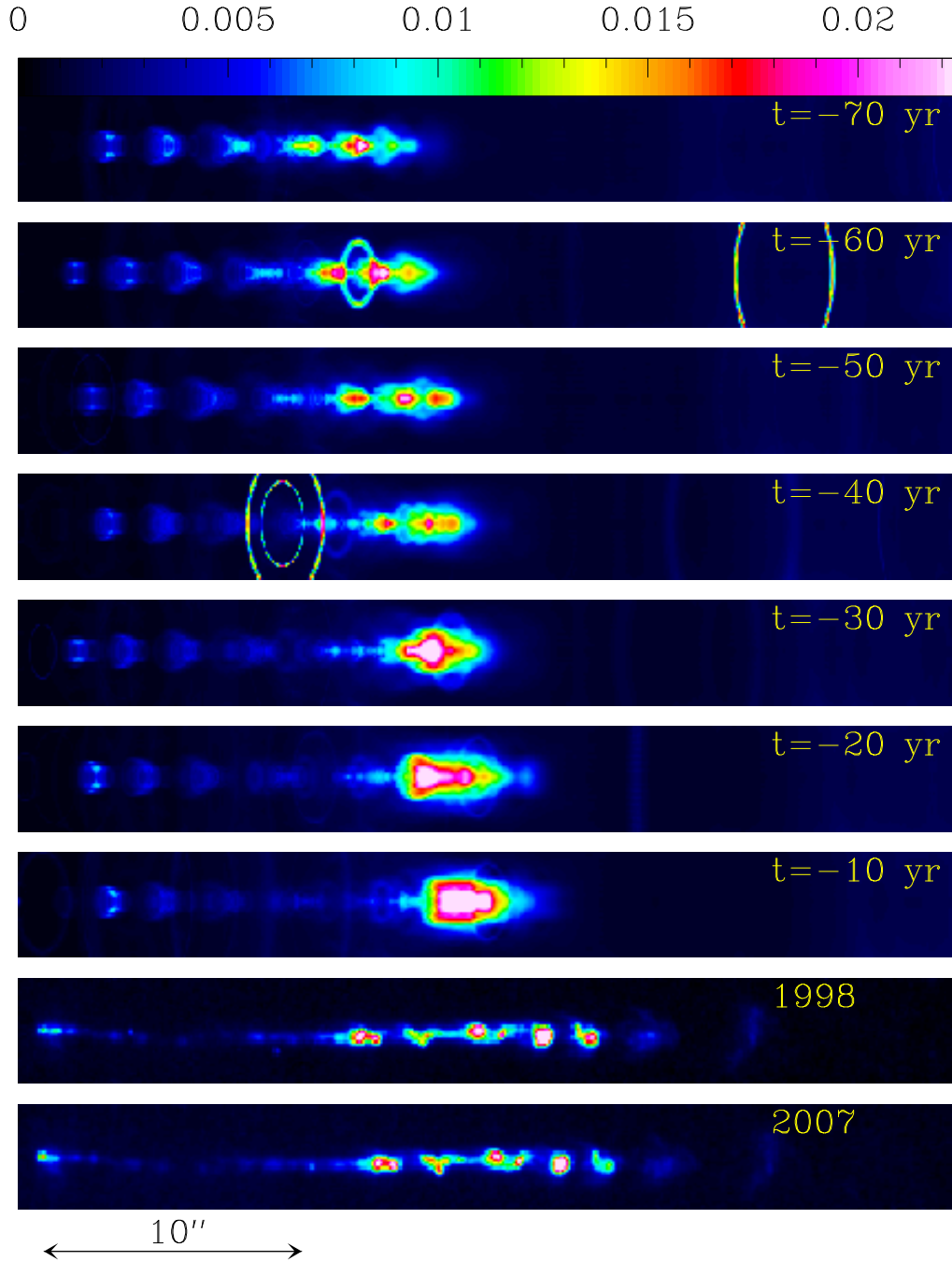


Fig. 8. [S II] 6716+30 intensity maps predicted from the  $\sigma = 0.75$ , 3-mode jet model for times  $t = -70$  to  $-10$  yr, at 10 yr intervals (the integration was started at  $t = -3000$  yr, see § 4). The two bottom frames show the [S II] images obtained with the HST in 1998 and 2007 (see § 2). The predicted maps have been computed assuming that the outflow axis lies at a  $30^\circ$  angle with respect to the plane of the sky (as appropriate for HH 34), and show a region with the source on the left and an axial extent of  $2.46 \times 10^{17}$  cm. The HH 34 [S II] maps has been scaled to the same scale as the predicted maps, assuming a distance of 450 pc (the displayed region has a horizontal size of  $36''.5$ ). The intensities of the predicted maps are shown with a linear color scheme (given in  $\text{erg s}^{-1} \text{cm}^{-2} \text{sterad}^{-1}$  by the top bar), and the HH 34 maps are shown with a linear color scheme with a maximum value corresponding to 0.2 counts per second per pixel. The color figure can be viewed online.

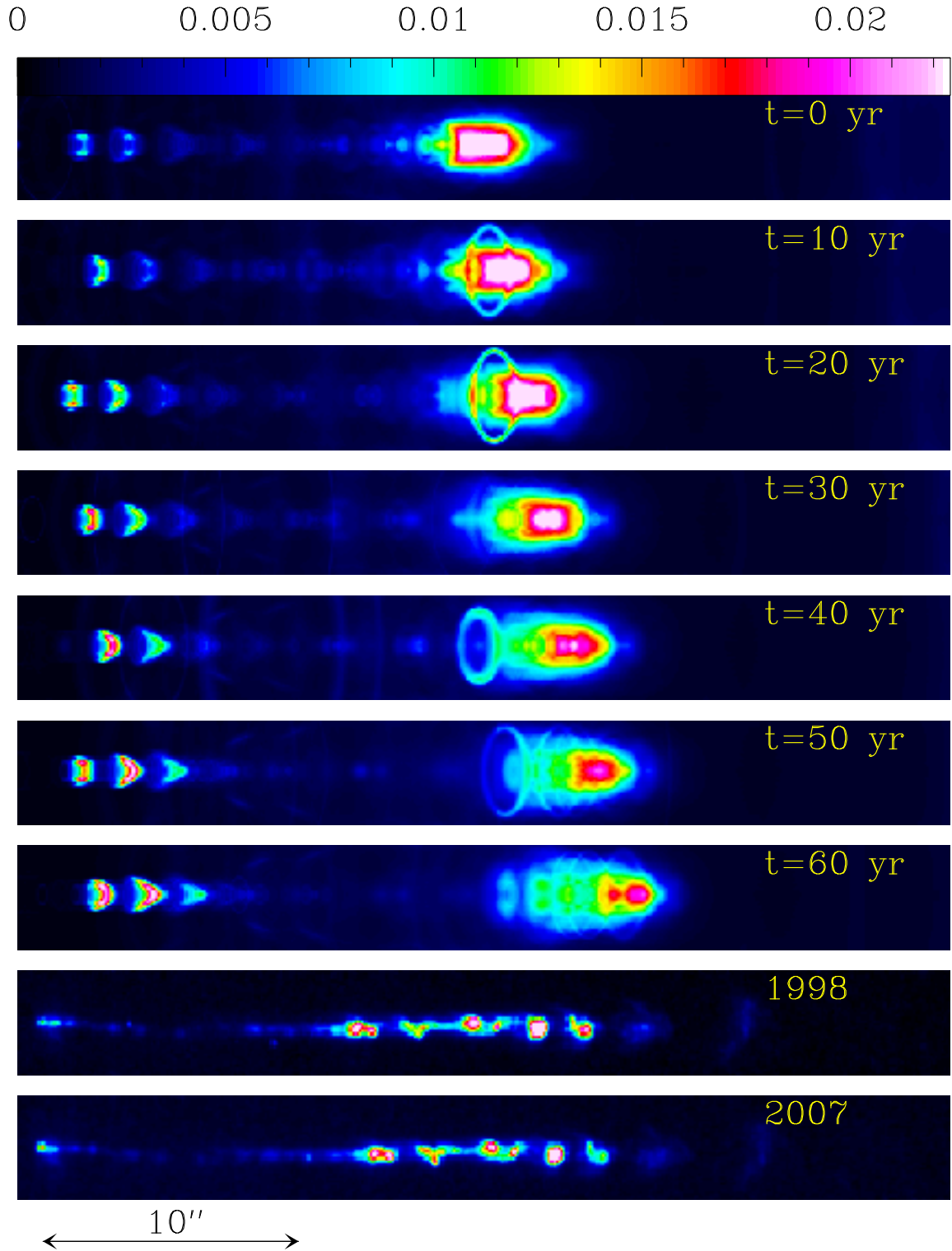


Fig. 9. The same as Figure 9, but with the intensity maps predicted from the  $\sigma = 0.75$ , 3-mode jet model for the times  $t = 0$  to 60 yr, at 10 yr intervals (see § 4). The color figure can be viewed online.

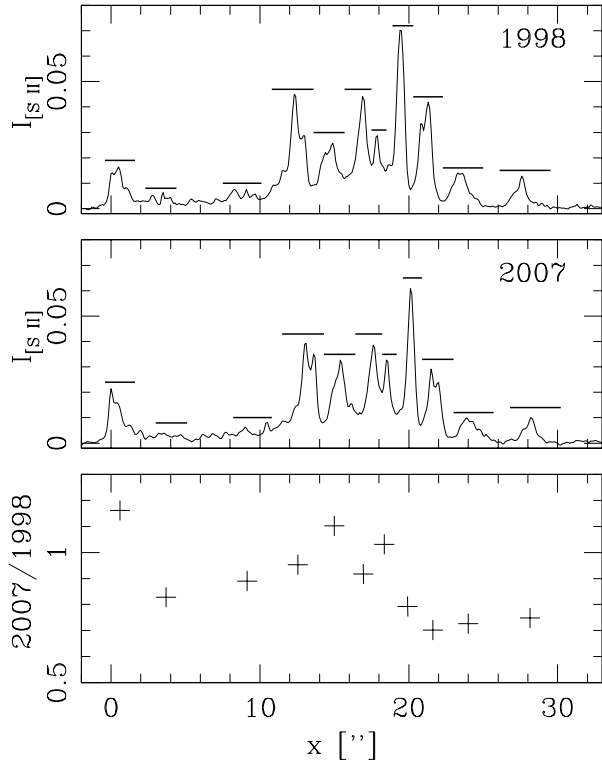


Fig. 10. [S II] tracings along the HH 34 jet for the 1998 (top) and 2007 (center) epochs, obtained by averaging over  $3''$  across the jet axis. The adjacent background emission has been subtracted. We have integrated the intensity over segments along the tracings. The lengths and positions of the segments are shown on the two intensity tracings, with a displacement of  $+0''.7$  along the  $x$ -axis for the 2007 epoch, (except for the segment incorporating the source, which was not displaced). The ratios between the integrated intensities (in the segments defined above) in the two epochs are shown in the bottom plot. The  $x$ -axis is the distance (in arcseconds) from the HH 34 source.

the HH 34 jet, and that the predicted structures show variabilities over  $\approx 10$  yr intervals which are consistent with the observed variability of the knots in HH 34.

The success we have obtained in reproducing the chain of knots within the first  $\sim 1'$  of the HH 34 jet is limited, as we are clearly not yet able to even attempt to carry out a quantitative comparison between the predicted and the observed emission structures. Nevertheless, the results are reasonably encouraging, because the predicted knot structures do show general morphologies and time-variabilities which appear to be consistent with the properties of the HH 34 knots. Also, the simulations approx-

imately reproduce the shape of the HH 34S bow shock, and the intensity contrast between this bow shock and the chain of aligned knots. In particular, we find that including a non-top hat ejection velocity cross section (with a moderate edge-to-center velocity ratio) improves the qualitative similarity between predicted and observed knot structures. If this result is to be taken at face value, it would imply that the HH 34 jet has a centrally peaked velocity profile, with a drop of  $\sim 25\%$  towards the edge of the jet (this outer edge representing a sharp boundary at which the jet beam is interrupted).

This result, however, is uncertain. It has been shown that the presence of a toroidal magnetic field (De Colle et al. 2008), and/or the presence of a multi-mode (possibly chaotic) ejection variability can lead to the formation of elongated IWS (De Colle 2011). In future work, it will be necessary to explore whether or not these possibilities produce knot morphologies and time-variations similar to the ones observed in the HH 34 jet.

This work is part of an ongoing effort to attempt to reproduce the observational characteristics of a set of specific HH jets with variable jet models. We have previously presented models for HH 34 (Raga & Noriega-Crespo 1998; Raga et al. 2002; Masciadri et al. 2002a), HH 111 (Masciadri et al. 2002b), HH 32 (Raga et al. 2004), HH 30 (Esquivel, Raga, & De Colle 2007), the DG Tau microjet (Raga et al. 2001) and the photoionized jet HH 444 (López Martín et al. 2001; Raga, Riera, & González-Gómez 2010). This kind of comparison between predictions from numerical simulations and observations should eventually provide the grounds for deciding which HH objects have emitting structures that are definitely the result of an ejection time-variability. It should also provide constraints on models for the ejection of HH jets and at the same time give us an understanding of the mechanisms by which the emitting structures are formed.

As a final point, we should note that our study of non-top hat ejection velocity jets is limited to quadratic cross sections. The choice of a quadratic velocity cross section is to some extent natural, because it can be thought of as a second order Taylor series of an arbitrary, flat-topped function. For this reason, most of the previous papers on HH jet models with non-top hat velocity cross sections have considered quadratic profiles (for example, Völker et al. 1999; Rosen & Smith 2003, 2004). Another natural choice for the functional form of the ejection velocity cross section would be a Gaussian, as this is the form of the velocity cross section of turbulent labo-

ratory jets. However, for the edge-to-center velocity ratios  $\sigma$  used in the present paper, the deviations between a Gaussian and a quadratic cross section are not very large (they are smaller than 6, 14 and 21% for  $\sigma = 0.75, 0.5$  and  $0.25$ , respectively). We would therefore not expect to obtain significantly different results for Gaussian cross sections.

This work was supported by the Conacyt grants 61547, 101356 and 101975. We acknowledge the support of E. Palacios of the ICN-Universidad Nacional Autónoma de México computing staff. We also thank an anonymous referee for helpful comments.

#### REFERENCES

- Cantó, J., Raga, A. C., & D'Alessio, P. 2000, *MNRAS*, 313, 656
- De Colle, F. 2011, in *IAU Symp. 275, Jets at all Scales*, ed. G. A. Romero, R. A. Sunyaev, & T. Belloni (Cambridge: Cambridge Univ. Press), 392
- De Colle, F., Raga, A. C., & Esquivel, A. 2008, *ApJ*, 689, 302
- Dennis, T. J., Cunningham, A. J., Frank, A., Balick, B., Blackman, E. G., & Mitran, S. 2008, *ApJ*, 679, 1327
- Esquivel, A., Raga, A. C., Cantó, J., & Rodríguez-González, A. 2009, *A&A*, 507, 855
- Esquivel, A., Raga, A. C., & De Colle, F. 2007, *A&A*, 468, 613
- Frank, A., Lery, T., Gardiner, T. A., Jones, T. W., & Ryu, D. 2000, *ApJ*, 540, 342
- Gardiner, T. A., & Frank, A. 2000, *ApJ*, 545, L153
- Hartigan, P., & Raymond, J. C. 1993, *ApJ*, 409, 705
- Heathcote, S., & Reipurth, B. 1992, *AJ*, 104, 2193
- Kajdic, P., Velázquez, P. F., & Raga, A. C. 2006, *RevMexAA*, 42, 217
- López-Martín, L., Raga, A. C., López, J. A., & Meaburn, J. 2001, *A&A*, 371, 1118
- Masciadri, E., de Gouveia Dal Pino, E. M., Raga, A. C., & Noriega-Crespo, A. 2002a, *ApJ*, 580, 950
- Masciadri, E., Velázquez, P. F., Raga, A. C., Cantó, J., & Noriega-Crespo, A. 2002b, *ApJ*, 573, 260
- Raga, A. C., & Biro, S. 1993, *MNRAS*, 264, 758
- Raga, A. C., Cabrit, S., Dougados, C., & Lavalley, C. 2001, *A&A*, 367, 959
- Raga, A. C., Cantó, J., Binette, L., & Calvet, N. 1990, *ApJ*, 364, 601
- Raga, A. C., Cantó, J., & Cabrit, S. 1998, *A&A*, 332, 714
- Raga, A. C., Cantó, J., De Colle, F., Esquivel, A., Kajdic, P., Rodríguez-González, A., & Velázquez, P. F. 2009, in *Protostellar Jets in Context*, ed. K. Tsinganos, T. Ray, & M. Stute (Berlin: Springer), 295
- Raga, A. C., De Colle, F., Kajdic, P., Esquivel, A., & Cantó, J. 2007, *A&A*, 465, 879
- Raga, A. C., & Noriega-Crespo, A. 1998, *AJ*, 116, 2943
- Raga, A. C., Riera, A., & González-Gómez, D. I. 2010, *A&A*, 517, 20
- Raga, A. C., Riera, A., Masciadri, E., Beck, T., Böhm, K. H., & Binette, L. 2004, *AJ*, 127, 1081
- Raga, A. C., Velázquez, P. F., Cantó, J., & Masciadri, E. 2002, *A&A*, 395, 647
- Rees, M. J. 1978, *MNRAS*, 184, 61
- Reipurth, B. 1989, *Nature*, 340, 42
- Reipurth, B., Bally, J., Graham, J. A., Lane, A. P., & Zealy, W. J. 1986, *A&A*, 164, 51
- Reipurth, B., Hartigan, P., Heathcote, S., Morse, J. A., & Bally, J. 1997, *AJ*, 114, 757
- Reipurth, B., & Heathcote, S. 1992, *A&A*, 257, 693
- Reipurth, B., Heathcote, S., Morse, J., Hartigan, P., & Bally, J. 2002, *AJ*, 123, 362
- Reipurth, B., Raga, A. C., & Heathcote, S. 1992, *ApJ*, 392, 145
- Rosen, A., & Smith, M. D. 2003, *MNRAS*, 343, 181
- \_\_\_\_\_. 2004, *MNRAS*, 347, 1097
- Smith, M. D., & Rosen, A. 2005, *MNRAS*, 357, 579
- Tesileanu, O., Massaglia, S., Mignone, A., Bodo, G., & Bacciotti, F. 2009, *A&A*, 507, 581
- Völker, R., Smith, M. D., Suttner, G., & Yorke, H. W. 1999, *A&A*, 343, 953
- Wilson, M. J. 1984, *MNRAS*, 209, 923

- F. De Colle: Astronomy and Astrophysics Department, University of California, Santa Cruz, CA 95064, USA (fabio@ucolick.org).
- P. Kajdic: Instituto de Geofísica, Universidad Nacional Autónoma de México, 04510 D.F., Mexico (primoz@geofisica.unam.mx)
- D. López-Cámara and A. C. Raga: Instituto de Ciencias Nucleares, Universidad Nacional Autónoma de México, Apdo. Postal 70-543, 04510 D.F., Mexico (raga@nucleares.unam.mx, diegorretas@gmail.com.)
- A. Noriega-Crespo: Spitzer Science Center, California Institute of Technology, Pasadena, CA 91125, USA (alberto@ipac.caltech.edu).